RSC Advances

PAPER

View Article Online
View Journal | View Issue

Cite this: *RSC Adv.*, 2025, **15**, 28841

N-doped CNT assisted GeO_2–Ge nanoparticles as a high-capacity and durable anode material for lithium-ion batteries

Erviani Rusman, Arunakumari Nulu and Keun Yong Sohn *

Germanium-based materials are emerging as promising anode candidates for lithium-ion batteries (LIBs) due to their high theoretical capacity, excellent electrical conductivity, and efficient lithium-ion diffusion at room temperature. However, their practical application is hindered by substantial volume changes during cycling, leading to poor cycling stability and diminished electrochemical performance. This study successfully created a GeO_2–Ge@NCNT composite using a cost-effective and environmentally friendly GeO_2 precursor through a hydrothermal method. N-doped carbon nanotubes (NCNT) were utilized to enhance electrochemical activity by providing additional active sites and improving structural stability. The GeO_2–Ge@NCNT anode demonstrated remarkable cycling stability with a capacity of 1017 mA h g^{-1} at a current density of 100 mA g^{-1} after 100 cycles, maintaining a coulombic efficiency of 98.15% and a capacity retention of 71.15% (*vs.* 2nd cycle discharge capacity). Moreover, C-rate analysis showed exceptional rate capability and consistent long-term cycling performance. This research presents a sustainable and scalable method for producing high-performance Ge-based anodes for next-generation lithium-ion battery technologies.

Received 28th March 2025
Accepted 7th July 2025

DOI: 10.1039/d5ra02163d

rsc.li/rsc-advances

1. Introduction

Recently, germanium (Ge)-based anodes have garnered considerable attention as promising electrode materials for lithium-ion battery (LIB) applications. This growing interest is driven by their superior electrochemical properties, including a high theoretical capacity of 1620 mA h g^{-1}, enhanced electrical conductivity relative to other group IV-A elements, a low operating voltage plateau, and a high lithium-ion diffusion coefficient at room temperature. Collectively, these attributes contribute to improved electrochemical performance of Ge-based anodes.[1–5] However, the practical application of Ge remains hindered by its inherently low-capacity retention and limited rate capability for lithium storage. A primary challenge stems from severe mechanical degradation of electrode contacts, which results in progressive capacity fading during lithiation/delithiation cycles. This issue is primarily attributed to substantial volumetric expansion and contraction associated with Li^+ insertion and extraction, ultimately compromising long-term cycling stability.[2,6–8] The repeated volumetric fluctuations in Ge structures lead to mechanical fracturing and continuous formation of solid electrolyte interphase (SEI) layers, which progressively isolate the active material from the current collector, thereby lowering electrochemical performance.[9–11]

Extensive research has been dedicated to hybrid materials to address the intrinsic limitations of Ge-based anodes to enhance structural stability and electrochemical performance. The synergistic integration of Ge and GeO_2 has demonstrated effectiveness in mitigating electrode pulverization. GeO_2 characterized by a high theoretical capacity of 2152 mA h g^{-1} has emerged as a promising candidate for anode applications.[12] During cycling, GeO_2 undergoes both conversion and alloying reactions, where the conversion reaction between Ge and Li_2O introduces an irreversible process that restricts lithium availability and contributes to capacity fading. It leads to high capacity, but with kinetic limitations.[13] However, the integration of Ge in GeO_2 acts as a catalyst for Li_2O decomposition, facilitating the formation of a core–shell structure, thereby enhancing lithium recovery and mitigating irreversible capacity loss. The Ge–Ge bond length within the shell remains identical to that observed in GeO_x crystals, whereas the oxygen shell exhibits a Ge–O bond length comparable to that in GeO_2. Nguyen *et al.* reported that a GeO_2/Ge composite synthesized *via* the reduction of GeO_2 using magnesium effectively mitigated volumetric expansion during cycling, thereby maintaining a stable capacity of 520.2 mA h g^{-1} after 40 cycles.[14]

$$GeO_2 + 4Li^+ + 4e^- \rightarrow Ge + 2Li_2O \text{ (conversion)}$$

$$Ge + xLi^+ + xe^- \rightarrow Li_xGe\ (0 \leq x \leq 4.4) \text{ (alloying)}$$

Department of Nanoscience and Engineering, Inje University, 197 Imje-ro, Gimhae, Gyeongnam-do, 50834, Republic of Korea. E-mail: ksohn@inje.ac.kr

Several strategies have been explored to improve structural stability and mitigate the adverse effects of volumetric expansion during cycling, including carbonaceous composites, nanostructure, and morphological reconstruction of nanomaterials.[15,16] The integration of carbon matrices has emerged as a particularly effective and scalable approach for enhancing cycle stability. Carbon functions as an electrolyte-blocking layer and a dispersing agent, preventing nanosized Ge particle aggregation during repeated charge/discharge cycles. Carbonaceous materials serve as volumetric buffers, alleviating mechanical stress, improving electrical conductivity, and suppressing electrode pulverization.[17–19] The integration of conductive carbon within nanocomposite materials significantly enhances charge transport kinetics by shortening lithium-ion diffusion pathways, thereby contributing to superior cycling stability.[20–22]

Among various carbon-based materials, carbon nanotubes (CNT) have garnered significant attention due to their high thermal stability, large surface area, and exceptional electrical conductivity.[23,24] Kaewraung *et al.* demonstrated the effectiveness of CNT incorporation in a Ge–Fe/MWCNT anode synthesized *via* a milling-assisted covalent-bonding method, achieving a reversible capacity of 925 mA h g^{-1} at 100 mA g^{-1} with an initial coulombic efficiency of 95% and outstanding capacity retention of 75%.[25] Furthermore, heteroatom doping using boron (B) and/or nitrogen (N) in CNT frameworks, has been shown to significantly enhance lithium-ion storage capacity, surface reactivity, and conductivity.[26,27] Specifically, nitrogen doping effectively tailors the intrinsic physicochemical properties of the carbon host, including structure surface and electronic characteristics, thereby improving electrochemical stability and long cycle life.[28] Despite the promising advantages of nitrogen-doped carbon in Ge-based anodes, research in this area remains limited, necessitating further investigations into this emerging strategy.

Prior studies have been conducted to enhance the structural stability and electrochemical performance of Ge-based anodes in LIB. Arro *et al.* synthesized a GeO_2/Ge/r-GO hybrid composite *via* a ball milling method, achieving a stable capacity of 300 mA h g^{-1} at a current density of 100 mA g^{-1} after 100 cycles.[29] Wang *et al.* reported that carbon doping in Ge-based anodes significantly enhances structural integrity, thereby improving cycling stability. This enhancement was attributed to the synergistic interaction between carbon and oxygen, which facilitated a more efficient lithiation process.[2] Additionally, Mei *et al.* employed electrospinning technology to fabricate a GeO_2–carbon nanofiber (GeO_2–CNF) composite. The result exhibited a high reversible capacity of 1034 mA h g^{-1} after 200 cycles at a current density of 100 mA g^{-1}.[11] Although electrospinning technology enables the synthesis of Ge-based anode materials with superior capacity, its widespread application is constrained by high production costs. Consequently, the development of cost-effective fabrication methods, such as hydrothermal synthesis represents a viable alternative for scalable production of Ge-based anode materials.

Herein, we propose the synthesis of a novel GeO_2–Ge@NCNT hybrid anode material using a cost-effective and non-toxic GeO_2 precursor *via* a hydrothermal method. Structural characterization confirmed the presence of Ge and GeO_2 lattices within the synthesized material. A comparative analysis between GeO_2–Ge and GeO_2–Ge@NCNT was conducted to evaluate the role of NCNT in enhancing cycling stability. The electrochemical results demonstrated that GeO_2–Ge@NCNT exhibited superior reversible capacity and cycling stability. These findings highlight the potential of GeO_2–Ge@NCNT as a potential high-capacity and durable anode material for next-generation lithium-ion batteries.

2. Result and discussion

Fig. 1 represents the schematic of the synthesis process for the GeO_2–Ge@NCNT composite *via* a hydrothermal. The GeO_2 was utilized as a cost-effective and environmentally benign precursor. The incorporation of prepared NCNT aimed to enhance the structural stability of the Ge-based material. During the annealing process, a partial reduction of oxygen within GeO_2 facilitated the *in situ* formation of Ge resulting in a GeO_2–Ge hybrid structure. The final composite exhibited a uniform distribution of NCNT within the carbon matrix, effectively surrounding the GeO_2–Ge core and reinforcing the overall structural integrity.

Fig. 2a presents the XRD pattern of the prepared nitrogen-doped carbon nanotubes (NCNT), exhibiting characteristic diffraction peaks at 25.83° and 42.54°, which correspond to (002) and (100) crystal plane of CNT (JCPDS: 96-101-1061). A small shift was observed at the (200) plane and a small impurity peak disappeared after N-doping identified no side reactions happened during the N-doped process.[30,31] Fig. 2b confirms the presence of GeO_2 and Ge in both GeO_2–Ge@NCNT and GeO_2–Ge samples. The diffraction peaks associated with Ge are observed at 28.28°, 53.44°, and 66.02°, corresponding to the crystal planes (111), (311), and (400), respectively (JCPDS: 98-004-4841). Furthermore, the sharp peaks attributed to GeO_2 were found at lattice index (100), (101), (110), (102), (111), and (200) which were identified as GeO_2 hexagonal (JCPDS: 98-005-3870).[14] Additionally, the diffraction peaks of NCNT in the GeO_2–Ge@NCNT composite overlap with the GeO_2 peaks at $2\theta = 25.83°$ and 42.54°. The presence of NCNT in the composite facilitates rapid electron transfer and enhances electrical conductivity, thereby contributing to the high electrochemical stability and capacity.[32]

The TGA result reveals the GeO_2–Ge@NCNT composite comprises approximately 12.7% carbon, as illustrated in Fig. 3a. An initial gradual weight loss of 1.66% is observed below 450 °C, which is attributed to the evaporation of residual organic solvents and the desorption of physically adsorbed water molecules. A rapid weight reduction occurs within the temperature range of 615–700 °C due to the thermal oxidation of carbon. Beyond 700 °C, the composite mass stabilizes, signifying the complete combustion of carbon and the absence of further decomposition processes.[2,33] The Raman spectrum of GeO_2–Ge@NCNT in Fig. 3b depicts two peaks at 1342 cm^{-1} and 1581 cm^{-1}, corresponding to D-band and G-band, respectively. The D-band indicated the structural defect, and the G-band

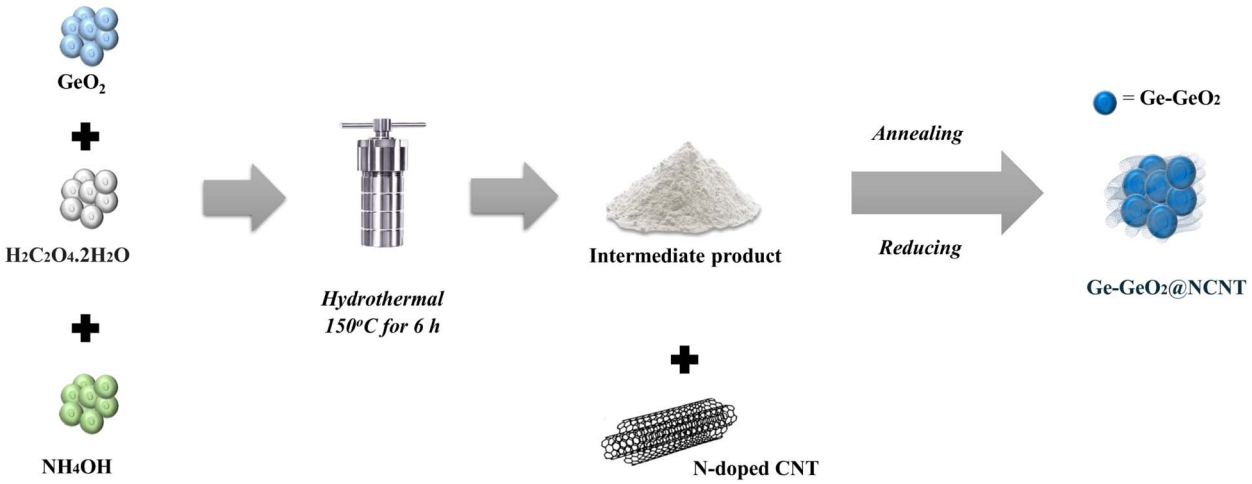

Fig. 1 Schematic of synthesis process of GeO_2–Ge@NCNT composite.

related to the graphitic carbon.[20] The intensity ratio of the D-band (I_D) and G-band (I_G) of GeO_2–Ge@NCNT was calculated to be 1.57. It suggests the composite contains more defect sites due to the interruptions sp^2 hybridized carbon framework, resulting in more active sites for Li^+ insertion which enhances specific capacity. Furthermore, the presence of 2D and D + D′ bands were reported at 2600–3000 cm^{-1} for the second-order overtone of the D band, suggesting the graphitized sp^2 carbon and combination mode revealing the structural defect in the carbon network. It indicates high electrical conductivity and the more active side of GeO_2–Ge@NCNT.[29]

The XPS analysis was carried out to evaluate the chemical bonding states within the GeO_2–Ge@NCNT composite. Fig. 4a exhibits the XPS spectrum with characteristic peaks at binding energies of 32.9 eV, 124.5 eV, 185.2 eV, 284.3 eV, 318.2 eV, 348.9 eV, and 532.8 eV, corresponding to Ge 3d, Ge 3p, Ge 3s, C 1s, Ge KLL, N 1s, and O 1s, respectively. The high-resolution XPS spectrum of O 1s (Fig. 4b) demonstrates three distinct peaks at 530.3 eV, 530.9 eV, and 531.4 eV are attributed to the O–Ge, C=C, and C–O functional groups, respectively. The high-resolution C 1s spectrum (Fig. 4c) displays peaks at 283.1 eV, 284.3 eV, 286 eV, and 289.6 eV, corresponding to the C–Ge, C–C, C–O, and C=O bonding states, respectively. The Ge 3d spectrum (Fig. 4d) exhibits multiple peaks at 30.4 eV, 31.2 eV, 31.8 eV, and 32.9 eV, indicating Ge–Ge, Ge–C, Ge–O, and Ge–N, respectively. The Ge–C functional group plays a crucial role in stabilizing GeO_2 during the lithiation/delithiation process, thereby improving structural integrity and overall electrochemical performance.[34] Furthermore, the high-resolution N 1s spectrum (Fig. 4e) identifies three characteristic peaks of pyridinic N, pyrrolic N, and graphitic N at 397.9 eV, 400.8 eV, and 403.2 eV, respectively. The spectrum of N 1s confirmed the successful N-doping in NCNT elaborating Li^+ diffusion properties in the Ge-based composite.

SEM and TEM analysis was conducted to investigate the morphological characteristics of the GeO_2–Ge@NCNT composite. Fig. S1 illustrates that the NCNT's nanotubular structure uniformly encapsulates GeO_2–Ge particles. The GeO_2–

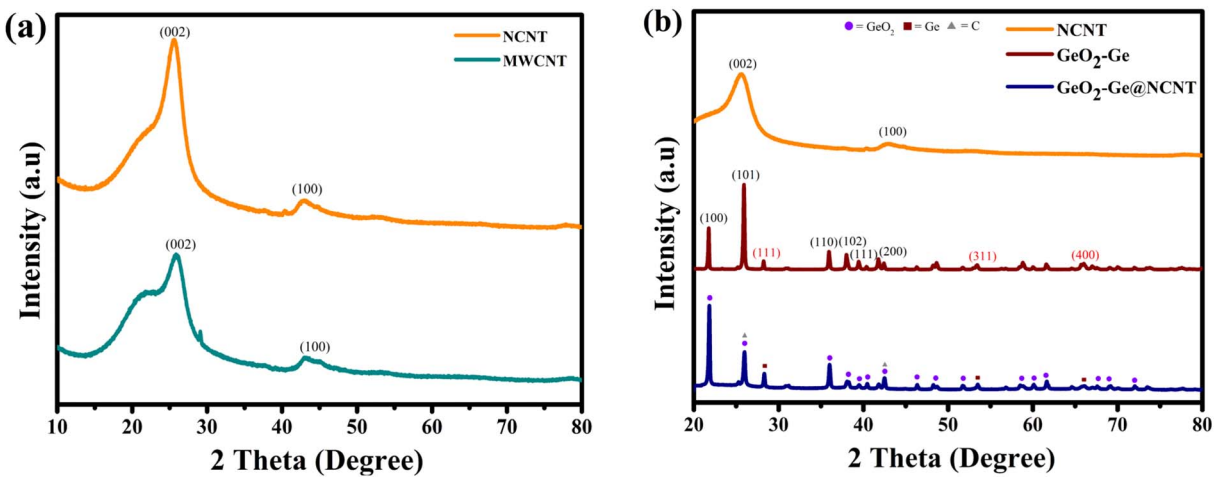

Fig. 2 XRD pattern for (a) NCNT and MWNCNT and (b) NCNT, GeO_2–Ge and GeO_2–Ge@NCNT.

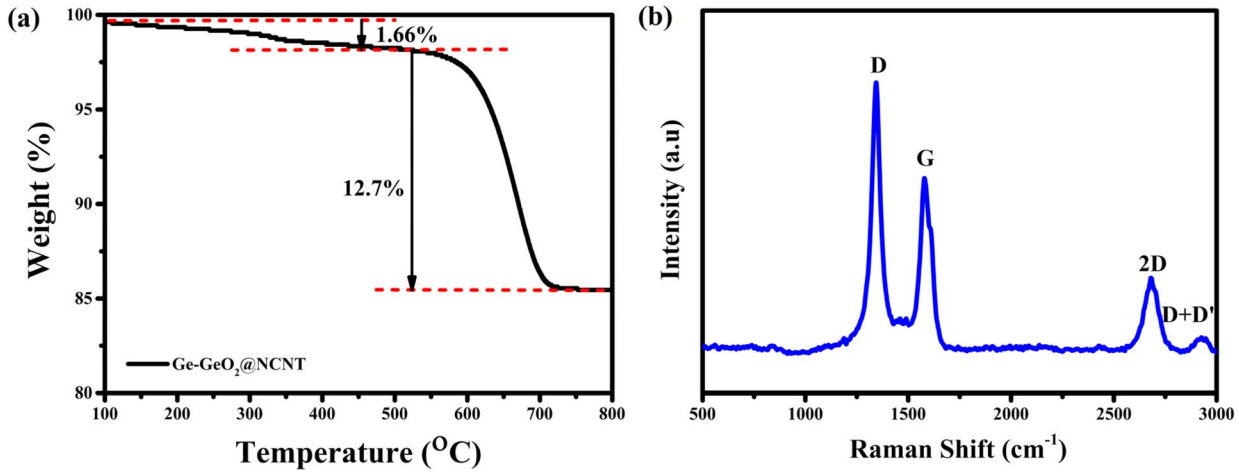

Fig. 3 (a) TGA analysis and (b) Raman spectrum for GeO_2–Ge@NCNT.

Ge domains have a spherical shape, with an average particle size of 400–700 nm, indicating uniform dispersion throughout the composite matrix. As shown in Fig. 5, the GeO_2–Ge particles are surrounded by NCNT, indicating a well-integrated composite structure. Fig. 5b confirms the presence of NCNT within the composite with tubular structures as highlighted by the yellow arrow. The darker regions observed in Fig. 5c indicate oxygen-rich areas, further corroborated by energy-dispersive X-ray spectroscopy (EDX) analysis. The selected regions from high-resolution TEM (HR-TEM) in Fig. 5d was examined in detail to determine the crystal lattice spacing using lattice fringe analysis. As depicted in Fig. 5e and f, the lattice fringe patterns revealed interplanar spacings of 0.327 nm and 0.33 nm, corresponding to the Ge (111) and GeO_2 (101) crystal planes, respectively.

Fig. 6a–e reports EDX mapping which confirmed the presence of C, N, Ge, and O elements in the synthesized GeO_2–Ge@NCNT composite. The uniform distribution of nitrogen which overlaps with carbon verifies the successful incorporation of NCNT in the GeO_2–Ge structure. The elemental composition is further supported by the EDX spectrum of GeO_2–Ge@NCNT, as depicted in Fig. 6f. The specific percentages of elemental composition of the GeO_2–Ge@NCNT composite are summarized in Table 1.

The galvanostatic charge/discharge profile of the GeO_2–Ge@NCNT composite was evaluated at a current density of 100 mA g^{-1} within a voltage window of 0.01–2.00 V *vs.* Li/Li^+, as depicted in Fig. 7a and b. The charge/discharge profile of GeO_2–Ge (Fig. 7a) demonstrates initial discharge and charge capacities of 2271 mA h g^{-1} and 1157 mA h g^{-1}, respectively. In contrast, Fig. 7b displays the corresponding profiles for GeO_2–Ge@NCNT, revealing initial discharge and charge capacities of 2198 mA h g^{-1} and 1351 mA h g^{-1}, respectively, resulting in an initial coulombic efficiency (CE) of 61.47%. The relatively low CE observed in the first cycle is primarily ascribed to the development of the solid electrolyte interphase (SEI) layer and the irreversible Ge–Li alloying reaction.[2,34] During the second cycle, the discharge/charge capacities of GeO_2–Ge and GeO_2–Ge@NCNT are recorded as 1260/1216 mA h g^{-1} and 1429/1367 mA h g^{-1}, respectively, with corresponding CE values of 96.54% and 95.64%. GeO_2–Ge composite exhibits a more capacity loss between the first and second cycles compared to the GeO_2–Ge@NCNT composite, highlighting the role of NCNT in improving cycling stability. After 100 cycles, the discharge/charge capacities of GeO_2–Ge and GeO_2–Ge@NCNT decrease to 344/342 mA h g^{-1} and 1017/1002 mA h g^{-1} with capacity retention values of 27.23% and 71.15%, respectively. These results indicate that NCNT effectively stabilizes the active material by mitigating volume expansion and suppressing capacity degradation during Li^+ insertion/extraction reaction, thereby enhancing the structural integrity and electrochemical performance.

Fig. 7c presents a comparative analysis of the long-term cycling performance of CNT, GeO_2–Ge, and O_2–Ge@NCNT electrodes. The GeO_2–Ge electrode exhibits the highest initial discharge capacity of 2271 mA h g^{-1} among the tested electrodes. However, a rapid capacity reduction is observed with the discharge capacity declining to 345 mA h g^{-1} after 100 cycles, corresponding to a capacity retention of only 27.37%. This significant capacity fading is primarily attributed to the extensive volume expansion during the lithium insertion/extraction process, which induces structural fractures and particle pulverization. In contrast, the NCNT electrode demonstrates superior structural stability over 100 cycles but low capacity. Consequently, NCNT is a promising dopant for GeO_2–Ge, reinforcing the composite structure and mitigating large-scale fractures during the lithiation/delithiation process. As a result, the GeO_2–Ge@NCNT composite exhibits markedly enhanced cycling performance compared to GeO_2–Ge and NCNT. After 100 cycles at a current density of 100 mA g^{-1} within a voltage range of 0.01–2.00 V, GeO_2–Ge@NCNT retains a high reversible discharge capacity of 1017 mA h g^{-1} with a remarkable coulombic efficiency exceeding 98.58% and a capacity retention of 71.15%.

Fig. 7d exhibits the rate performance tests conducted at varying current densities of 0.1, 0.2, 0.4, 0.8, and 1.6 A g^{-1}. The

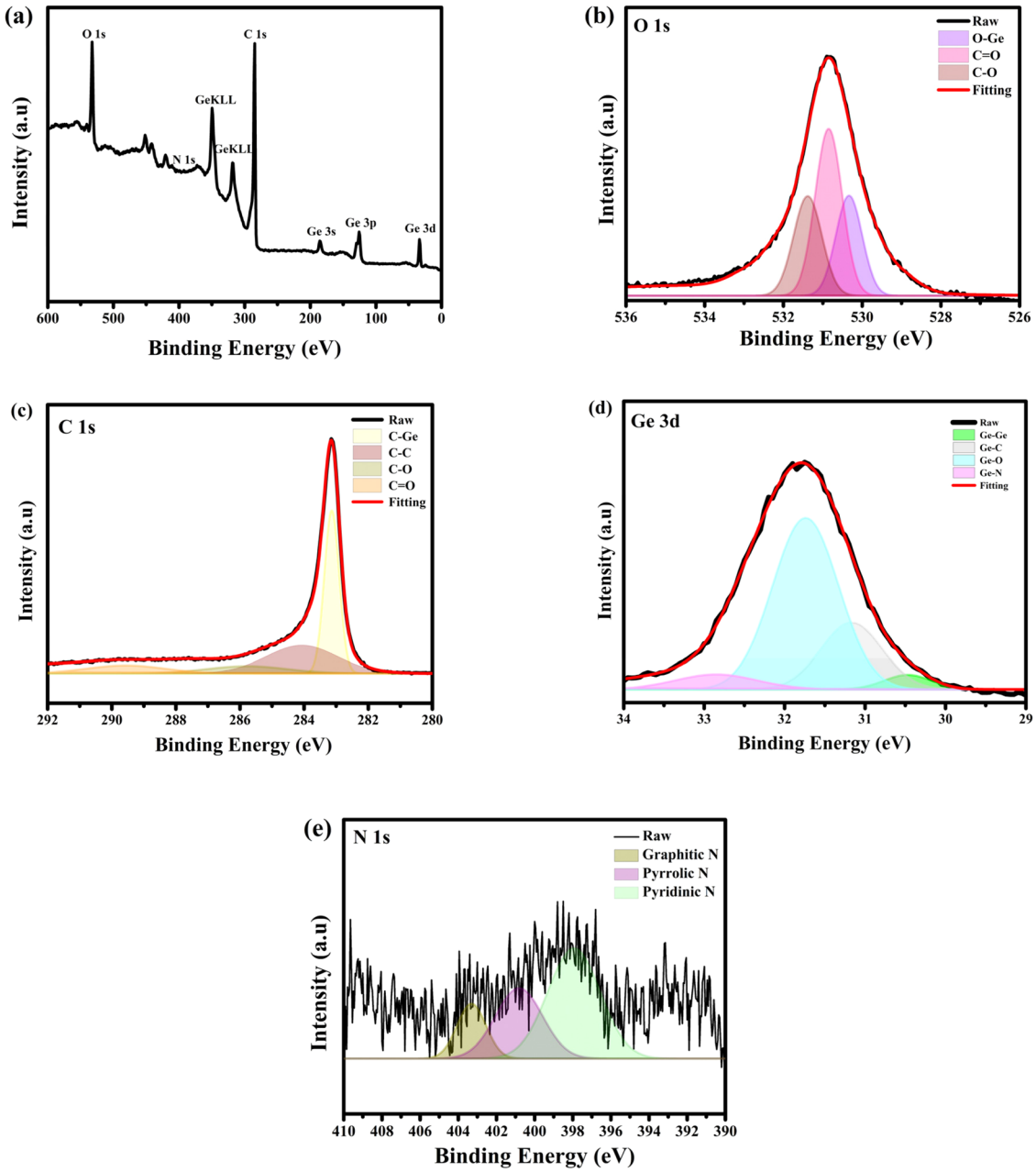

Fig. 4 XPS spectra (a) survey scan of GeO_2–Ge@NCNT; high-resolution XPS spectrum of (b) O 1s, (c) C 1s, (d) Ge 3d, and (e) N 1s in GeO_2–Ge@NCNT.

GeO_2–Ge@NCNT composite demonstrates excellent recovery of reversible capacity when the current density is reduced from 1.6 A g^{-1} to 0.1 A g^{-1}. Following high-rate cycling, GeO_2–Ge@NCNT shows an impressive reversible capacity of 1006 mA h g^{-1} and stabilizes around 1100 mA h g^{-1} at 0.1 A g^{-1}. These results highlight the effectiveness of NCNT incorporation in stabilizing the Ge-based composite, thereby significantly improving both electrochemical performance and long-term cycle stability.

The rate capability performance of the electrodes at varying current densities was evaluated, as depicted in Fig. 8a and b. The charge–discharge profiles provide a comparative analysis of the rate capacities of GeO_2–Ge and GeO_2–Ge@NCNT during the first cycle across a range of current densities from 0.1 A g^{-1} to 1.6 A g^{-1}. As illustrated in Fig. 8a, the reversible capacities of the GeO_2–Ge electrode at increasing current densities of 0.1, 0.2, 0.4, 0.8, and 1.6 A g^{-1} are recorded as 2354, 1094, 823, 589, and 240 mA h g^{-1}, respectively. A sharp decline in capacity at high current densities indicates the structural instability of GeO_2–Ge, where severe mechanical stress and structural fracturing lead to rapid loss of capacity. Conversely, the GeO_2–Ge@NCNT composite demonstrates significantly improved rate capability and structural stability under high-current conditions. As shown in Fig. 8b, the GeO_2–Ge@NCNT electrode exhibits

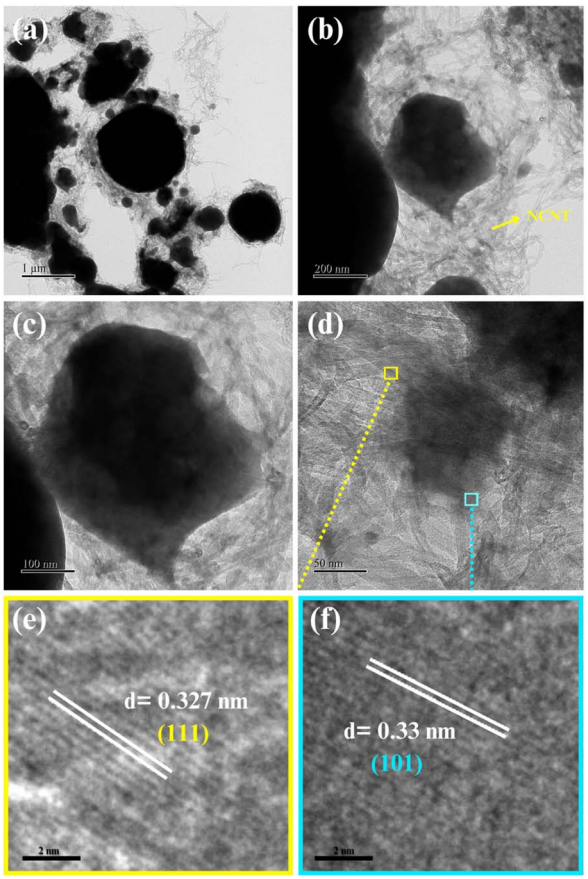

Fig. 5 TEM image of GeO_2–Ge@NCNT in different magnifications: (a) 1 μm, (b) 200 nm, (c) 100 nm, (d) HR-TEM image, and (e and f) lattice fringes of a selected area from image (d).

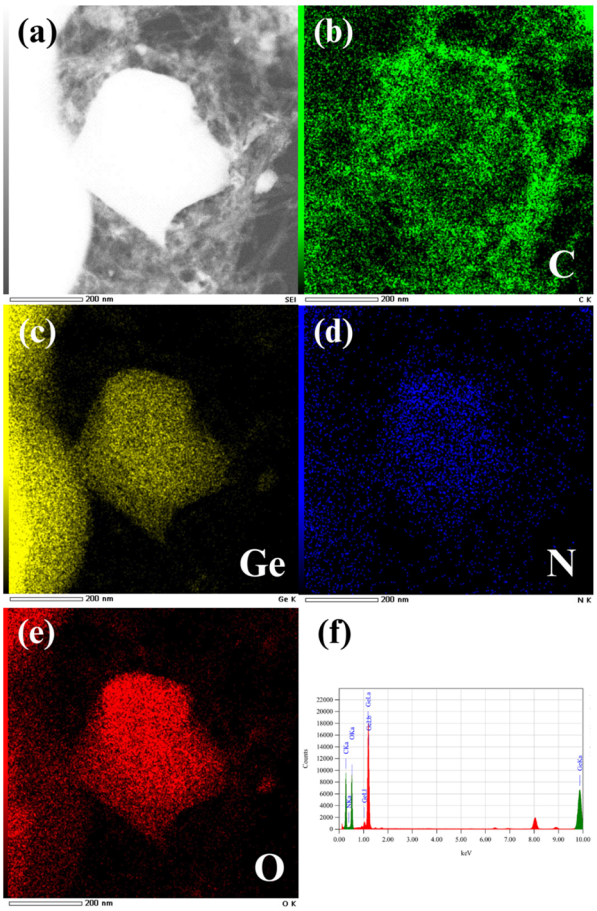

Fig. 6 (a) STEM images and corresponding EDX elemental mapping, indicating (b) C, (c) Ge, (d) N, (e) O signal mapping of GeO_2–Ge@NCNT image, and (f) EDX pattern of GeO_2–Ge@NCNT.

superior reversible capacities of 2165, 1221, 1069, 903, and 699 mA h g^{-1} at current densities of 0.1, 0.2, 0.4, 0.8, and 1.6 A g^{-1}, respectively. These findings underscore the critical role of NCNT incorporation in enhancing electrical conductivity, facilitating Li-ion diffusion, and stabilizing the electrochemical cycling process, particularly under high-rate conditions.

Fig. 9a and b illustrate the cyclic voltammetry (CV) profiles of the GeO_2–Ge and GeO_2–Ge@NCNT electrodes, recorded over a voltage range of 0.01–2.00 V. The formation of the solid electrolyte interphase (SEI) during the initial lithiation process consequently affected the distinct features observed in the cyclic voltammetry (CV) curves during the first cycle for both electrodes.[35] As depicted in Fig. 9a, the GeO_2–Ge electrode exhibits two prominent oxidation peaks. During the oxidation process, a sharp peak is observed at 0.55 V and a broader peak at 1.15 V. During the reduction process, a peak emerges at 0.13 V and an additional peak appears at 0.11 V after five cycles. These characteristic peaks correspond to the alloying reaction between Ge and Li^+ and the conversion reaction of GeO_2, which typically occurs within the voltage range of 0.11–0.50 V.[29,34]

Fig. 9b exhibits the CV profile of GeO_2–Ge@NCNT electrodes. During the delithiation process, two distinct peaks are observed at 0.45 V and 1.15 V. The sharp peak at 0.45 V

Table 1 Element quantitative in GeO_2–Ge@NCNT based on EDX mapping analysis

Element	Mass%	Atom%
C	29.41	59.12
N	0.53	0.91
O	14.18	21.40
Ge	55.88	18.57

corresponds to the oxidation of GeO_2. The increased intensity is likely due to a substantial transition from the deintercalation of Li^+ ions in the NCNT toward the more dominant Li–Ge dealloying process during delithiation. The broad peak at 1.15 V serves as an indicator of the oxidation of GeO_2. It suggests that Ge encapsulated within the NCNT matrix undergoes oxidation.[29,36,37]

The sharper and broader peaks observed in the GeO_2–Ge@NCNT electrode during the lithiation and delithiation processes indicate enhanced electrochemical kinetics facilitated by the NCNT network. This network improves charge transport and promotes structural stability.[38] In the reduction reaction, the CV scan reveals a peak at 0.11 V during the initial

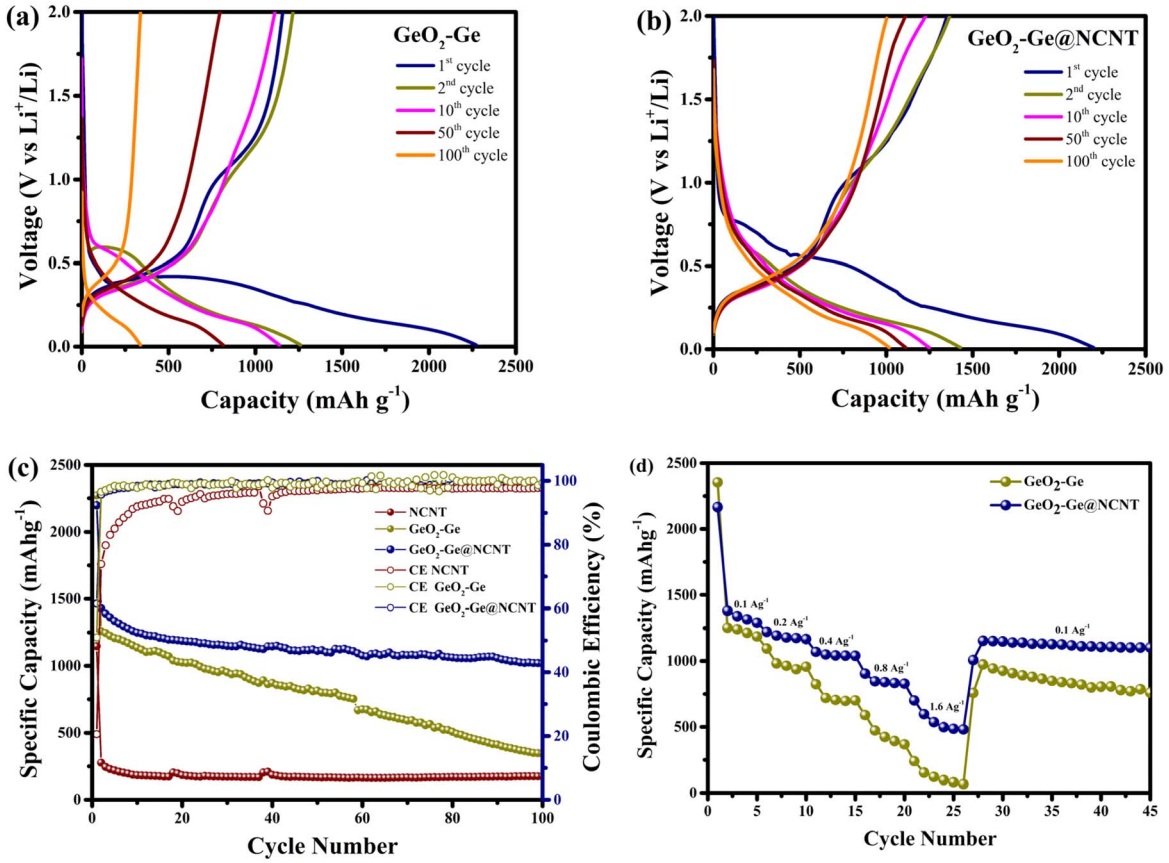

Fig. 7 Charging and discharging profile of (a) GeO_2–Ge and (b) GeO_2–Ge@NCNT at 100 mA g^{-1}, (c) cycling performance and coulombic efficiency of GeO_2–Ge and GeO_2–Ge@NCNT at current density 100 mA g^{-1}, and (d) rate performance at different current densities 0.1 A g^{-1} to 1.6 A g^{-1} for GeO_2–Ge and GeO_2–Ge@NCNT.

cycle, associated with the solid electrolyte interphase (SEI) layer formation. As cycling progresses, the intensity of this 0.11 V peak diminishes, while the sharp peak at 0.49 V intensifies, indicating the development of a stable SEI layer. Additionally, the decreasing peak intensity at 0.11 V confirms the lithiation of GeO_2, signifying the decomposition of GeO_2 and the initial formation of the Li–Ge alloying process.[39–41] Fig. 10 depicts the surface morphology change of GeO_2–Ge@NCNT before and after 100 cycles at 100 mA g^{-1}. The SEM images identified that the GeO_2–Ge@NCNT intensively retains the surface from extreme cracking formation, maintaining the electrode

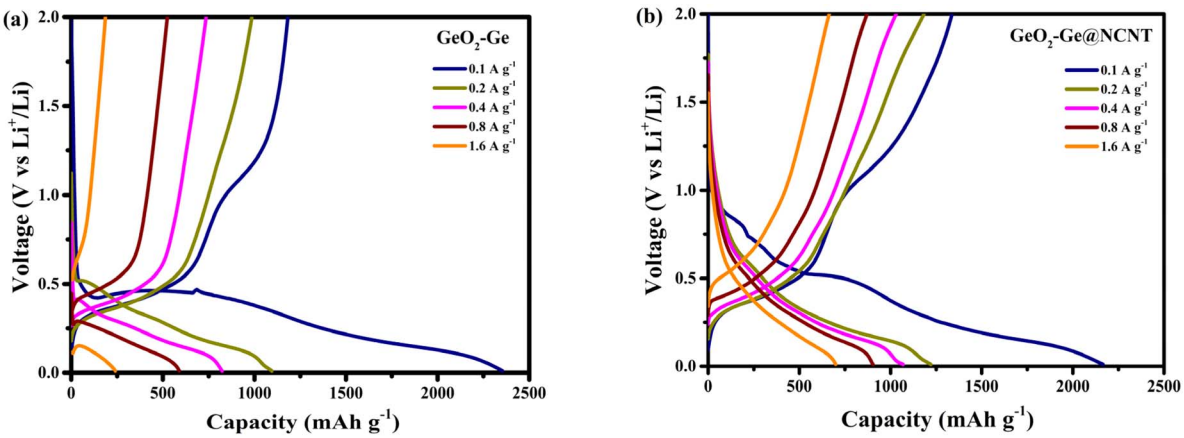

Fig. 8 Charging and discharging profile of (a) GeO_2–Ge and (b) GeO_2–Ge@NCNT at different C-rate (0.1–1.6 A g^{-1}) in the first cycle.

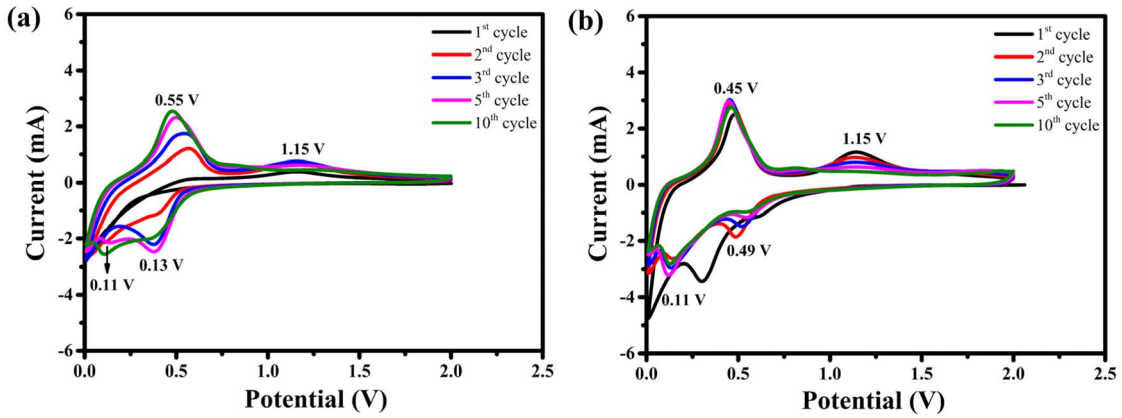

Fig. 9 CV curve for (a) GeO_2–Ge and (b) GeO_2–Ge@NCNT.

integrity, which leads to the electrode stability during the repeated lithiation–delithiation process.

XPS characterization conducted after electrochemical cycling offers detailed insights into the surface chemistry evolution of the GeO_2–Ge@NCNT electrode. Fig. S2 illustrates a pronounced increase in the O 1s peak intensity, along with the emergence of a distinct Li 1s signal, which is indicative of SEI as a key factor in stabilizing electrode–electrolyte interactions and ensuring long-term cycling performance in Li-ion batteries.[42,43] Simultaneously, a reduction in the C 1s and Ge 3d signal intensities reflects partial surface passivation due to SEI deposition and reaction product accumulation, which is commonly observed in conversion and alloying anodes.[44] The peaks at C 1s signal after long-term cycling were observed to be higher and clearer. The increasing intensity of group C–C and C=O in the C 1s signal supports the presence of organic species derived from electrolyte decomposition.[45] Moreover, the weak N 1s signal is shown to nearly disappear in the survey spectrum, and from the high-resolution XPS of the N 1s signal, only the pyridinic N function group was observed after long-term cycling. It suggests either encapsulation of the N functional group by SEI or degradation of the N-doped carbon framework. Despite these transformations, the presence of Ge 3d and Li 1s signals post-cycling confirms continued lithium storage activity, underscoring the electrochemical reversibility of the Ge-based phase. These findings collectively demonstrate that the GeO_2–Ge@NCNT architecture undergoes expected interfacial modifications while retaining functional lithium-reactive sites.

Fig. 11a presents a comparative analysis of the electrochemical resistance of GeO_2–Ge and GeO_2–Ge@NCNT based on Nyquist plots obtained from AC impedance spectroscopy. The tilted line at the low-frequency range corresponds to the diffusion of lithium kinetics to the electrode. In addition, semi-cycle at the middle and high-frequency range refers to charge transfer resistance in the electrode and electrolyte interface.[46] The total resistance of GeO_2–Ge@NCNT before cycling is lower (257 Ω) than that of GeO_2–Ge (351 Ω), which is primarily attributed to the incorporation of NCNT. The introduction of NCNT in composite enhances electrical conductivity and facilitates more efficient redox kinetics.[1,47] The impedance characteristics illustrated in Fig. 11b further depict Nyquist plots for GeO_2–Ge and GeO_2–Ge@NCNT after 10 cycles. A reduction in resistance is observed for both electrodes after cycling, where GeO_2–Ge@NCNT shows a more significant decrease. This result confirms its enhanced structural stability and improved

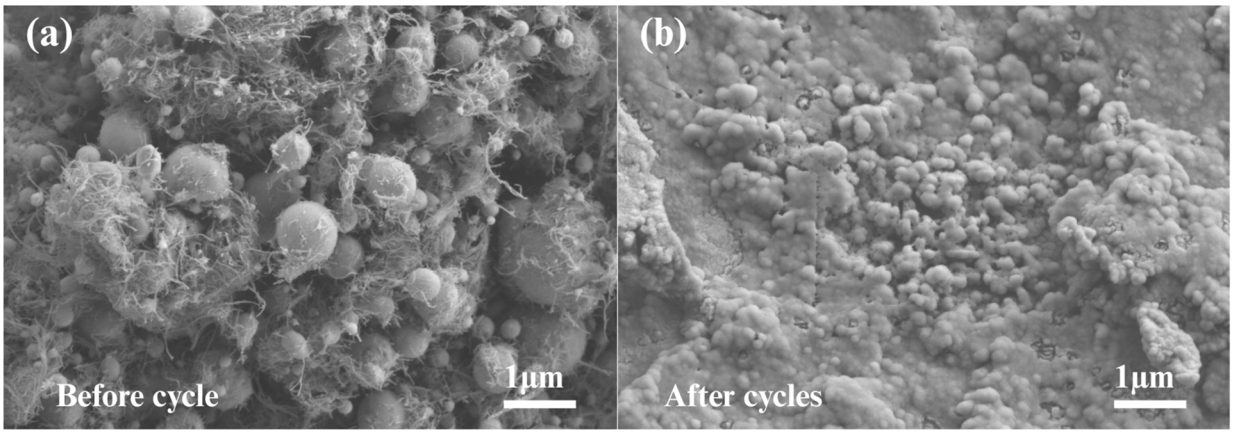

Fig. 10 SEM images of GeO_2–Ge@NCNT (a) before and (b) after 100 cycles at 100 mA g^{-1}.

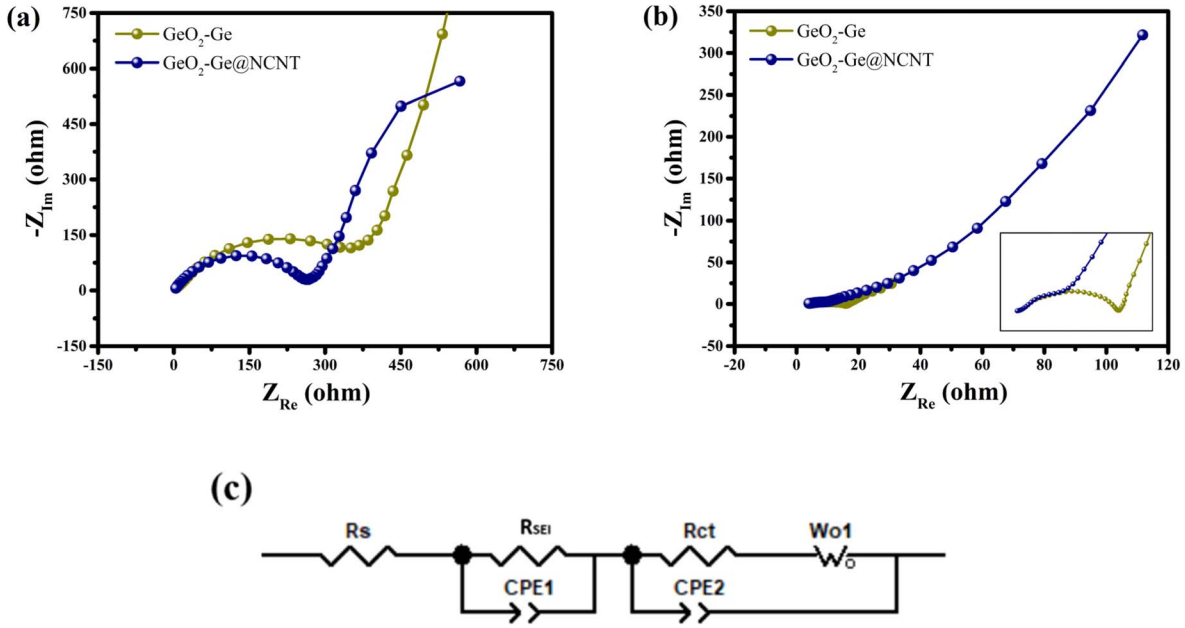

Fig. 11 Nyquist plots of AC impedance for GeO_2–Ge and GeO_2–Ge@NCNT (a) before cycling and (b) after 10 cycles, and (c) equivalent circuit model of EIS fitting curve.

Table 2 Values of the equivalent circuit components data of GeO_2–Ge and GeO_2–Ge@NCNT

	Before cycling			After 10 cycles		
Samples	R_s (Ω)	R_{SEI} (Ω)	R_{ct} (Ω)	R_s (Ω)	R_{SEI} (Ω)	R_{ct} (Ω)
GeO_2–Ge	12	124	215	5.6	4.8	5.3
GeO_2–Ge@NCNT	9.8	47.2	200	4	1.5	3.5

electrical conductivity during redox processes, thereby reinforcing its potential as an advanced anode material.

The equivalent circuit model from Fig. 11c consists of multiple resistance components: R_s represents the total resistance, encompassing electrolyte resistance, separator resistance, and electrical contact resistance. Furthermore, R_{SEI} and R_{ct} correspond to the resistance of the solid electrolyte interphase (SEI) layer and charge transfer resistance, respectively, while the constant phase elements C_{PE1} and C_{PE2} denote capacitance and charge transfer capacitance.[2,48] According to Table 2, the R_s and R_{ct} values of GeO_2–Ge@NCNT before cycling (9.8 Ω and 200 Ω) are less than that of GeO_2–Ge (12 Ω and 215 Ω), indicating a more efficient electron transport pathway facilitated by the superior conductivity of NCNT. Moreover, the R_{ct} of GeO_2–Ge@NCNT exhibits a substantial reduction after cycling, suggesting that NCNT effectively stabilizes the electrode structure and mitigates the depletion of active material. Thus, NCNT serves as an effective component in reducing electrolyte penetration and reinforcing the SEI layer during charge/discharge cycles, ultimately contributing to enhancing coulombic efficiency and capacity retention.[25,30] Compared with previous research related to Ge-based anodes, as reported in Table 3, GeO_2–Ge@NCNT provided high reversible capacity and

Table 3 Performance comparison between this work and prior research about Ge-based anodes

Electrode	Specific capacity (mA h g^{-1})	Current density (mA g^{-1})	Cycle	Ref.
GeO_2 CNF	1034	100	200	11
GeO_2/Ge	502.2	100	40	14
3D void/Ge@C	990	100	100	17
Ge–Fe/MWCNT	491	5000	1000	25
GeO_2/Ge/r-GO	300	100	100	29
GeO_x-coated rGO	758	2000	700	33
GeO_2/C	984.2	200	200	34
GeO_2/Ge	665.3	500	100	39
GeO_2@C	940	50	50	49
CNT–GeO_2	844.8	500	500	50
GeO_2–Ge@NCNT	1017	100	100	This work

excellent stability performance for long-term cycling which potentially supports it as durable anode material for LiB.

3. Conclusion

The GeO_2–Ge@NCNT composite was successfully synthesized using a cost-effective and non-toxic GeO_2 precursor. The incorporation of Ge within the composite significantly enhances structural stability as a catalyst for Li_2O decomposition. Additionally, the formation of Ge–C functional groups contributes to stabilizing GeO_2–Ge during the lithiation/delithiation process, thereby improving its structural integrity and sustaining a high capacity. Electrochemical assessments underscore the substantial contribution of NCNT in improving electrochemical kinetics and cycling stability during the charge/discharge processes. The GeO_2–Ge@NCNT electrode exhibited outstanding cyclic stability, maintaining the reversible capacity of 1017 mA h g^{-1} after 100 cycles with a coulombic efficiency of 98.15% and a capacity retention of 71.15%. The structural and electrochemical characterizations validated that the presence of NCNT facilitates rapid electron transport and enhances electrical conductivity, establishing GeO_2–Ge@NCNT as a promising high-capacity and durable anode material for lithium-ion batteries.

4. Experimental

4.1 Materials

GeO_2 (Kanto Chemical CO., INC, 99.99%), oxalic acid dihydrate ($H_2C_2O_4 \cdot 2H_2O$) (Kanto Chemical CO., Inc., 99.5%), melamine (DAEJUNG, 5652-4100), MWCNT (Hanwha Nanotech Corp. CM-100, diameter: 10–14 nm), ethanol (Sigma-Aldrich, ≥99.5%), and deionized water were used without any purification.

4.2 Preparation of N-doped CNT (NCNT)

Nitrogen-doped carbon nanotubes (NCNT) were synthesized by a solid-state method using MWCNT and melamine at a mass ratio of 1 : 3, respectively. Melamine served as the nitrogen precursor to facilitate doping. The mixture was homogenized *via* ball milling at 45 rps for 30 minutes to ensure uniform particle distribution. The resulting powder was annealed at 900 °C under N_2 atmosphere with a controlled heating rate of 5 °C min^{-1} for 1 h. After heat treatment, a black powder was obtained and labeled as NCNT.

4.3 Synthesis of GeO_2–Ge@NCNT

The GeO_2–Ge@NCNT composite was synthesized *via* a hydrothermal method, as illustrated in Fig. 1. The commercial GeO_2 was utilized as the precursor. Specifically, 425 mg of GeO_2 and 1.2 g of $H_2C_2O_4 \cdot 2H_2O$ were dissolved in a mixture of 10 mL ammonia and 30 mL deionized water under continuous stirring for 1 h to achieve a homogeneous solution. The solution was transferred to a 100 mL Teflon autoclave and hydrothermal treated at 150 °C for 6 h. The precipitate was collected and washed multiple times with ethanol using centrifugation. The intermediate product was obtained after vacuum drying at 80 °C overnight. The GeO_2–Ge@NCNT was fabricated as follows: the intermediate product was mixed with NCNT at a mass ratio of 9 : 1 and dispersed in 7 mL of ethanol, followed by stirring for 1 h to ensure uniform dispersion. The obtained precipitate was collected and vacuum-dried at 80 °C for 12 h. The dried powder was subsequently annealed at 700 °C under an Ar atmosphere with a heating rate of 5 °C min^{-1} for 2 h to get GeO_2–Ge@NCNT with black color. For comparison, GeO_2–Ge was synthesized following the same procedure without the addition of NCNT, yielding a final white-colored GeO_2–Ge powder.

4.4 Structural characterization

The structural properties of synthesized materials were characterized by XRD spectroscopy ((Shimadzu 700) with Cu Kα radiation at a wavelength (λ) 1.54 Å ($10° \leq 2\theta \leq 80°$), 40 kV, 30 mA, scan rate 2 min^{-1}, step size 0.02°). The thermal stability and quantity of elements present in the prepared material were evaluated *via* Thermogravimetric Analysis (TGA) (Shimadzu DSC-60/DTG-60), performed under an air atmosphere within a temperature range of 25 °C to 800 °C. X-ray Photoelectron Spectroscopy (XPS) was performed to characterize the elemental composition and element states. The morphological and microstructural characteristics were examined using Transmission Electron Microscopy (TEM) equipped with an energy-dispersive X-ray spectroscopy (EDX) detector (FE-TEM, JEOL JEM-F200).

4.5 Electrochemical measurement

The working electrode was fabricated by homogeneously mixing the as-synthesized active material, Super-P, and polyamide-imide (PAI) dissolved in *N*-methyl pyrrolidone (NMP) binder at a mass ratio of 70 : 15 : 15, respectively. The resulting slurry was uniformly coated onto a copper foil substrate using a doctor blade with a controlled thickness of 25 μm, followed by drying at 100 °C for 4 h. Subsequently, the electrode underwent vacuum heat treatment at 200 °C for 3 h to obtain the working electrode. Electrochemical characterization was conducted using a half-cell (CR2032) with mass loadings of 0.32 mg cm^{-2}, 2.32 mg cm^{-2}, and 2.5 mg cm^{-2} for NCNT, GeO_2–Ge, and GeO_2–Ge@NCNT electrodes, respectively. The electrodes were assembled in an argon-filled glove box. The lithium foil was employed as the counter electrode, a polypropylene membrane served as the separator, and 1 M $LiPF_6$ in ethylene carbonate (EC) and diethyl carbonate (DEC) (1 : 1 v/v) was used as the electrolyte. The electrochemical behaviors were investigated using a BioLogic battery testing instrument, where galvanostatic charge–discharge measurements were performed within a voltage range of 0.01–2.00 V. Cycling stability was assessed at a current density of 100 mA g^{-1}, while rate capability was analyzed across a range of 100–3200 mA g^{-1}. Cyclic voltammetry (CV) and electrochemical impedance spectroscopy (EIS) analyses were performed utilizing a BioLogic SP-150-127 electrochemical workstation. Impedance spectra were recorded over a frequency range of 10 mHz to 10 kHz, with an AC amplitude of ~5.02 mV. The specific capacities were calculated according to the weight of each active material.

Author contributions

Conceptualization, E. R.; methodology, E. R. and A. N.; measurement and analysis, E. R.; supervision, K. Y. S., and A. N.; writing – original draft preparation, E. R.; writing – review and editing, K. Y. S., E. R., and A. N.; project administration, K. Y. S. and A. N.; funding acquisition, K. Y. S. and A. N. All authors have read and agree to the published version of the manuscript.

Conflicts of interest

The authors declare that they have no known competing financial interests or personal relationships that could have appeared to influence the work reported in this paper.

Data availability

The data supporting this article have been included in the SI. EIS studies. See DOI: **https://doi.org/10.1039/d5ra02163d**.

Acknowledgements

This work was supported by the National Research Foundation of Korea (NRF) (grants 2021R1I1A1A01061270 and 2021R1I1A3059637), funded by the Ministry of Education.

References

1 Y. Zhaoa, Y. Li, T. Wang, X. Zhao, X. Kong, G. Li, Z. Wang, F. He, X. Chang, Z. Liu, L. Wu and P. Yang, *J. Colloid Interface Sci.*, 2025, **677**, 655–664.
2 G. Wang, H. Lei, Z. Yuan, L. Li, Z. Zhan and X. Wang, *J. Energy Storage*, 2024, **100**, 113757.
3 Y. Dong, B. Wang, K. Zhao, Y. Yu, X. Wang, L. Mai and S. Jin, *Nano Lett.*, 2017, **17**, 5740–5746.
4 L. Huang, G. H. Waller, Y. Ding, D. Chen, D. Ding, P. Xi, Z. Wang and M. Liu, *Nano Energy*, 2015, **11**, 64–70.
5 C. Kim, G. Hwang, J. W. Jung, S. H. Cho, J. Y. Cheong, S. Shin, S. Park and I. D. Kim, *Adv. Funct. Mater.*, 2017, **27**, 1605975.
6 C. M. Park, J. H. Kim, H. Kim and H. J. Sohn, *Chem. Soc. Rev.*, 2010, **39**, 3115–3141.
7 D. Larcher, S. Beattie, M. Morcrette, K. Edstrom, J. C. Jumas and J. M. Tarasco, *J. Mater. Chem.*, 2007, **17**, 3759–3772.
8 E. A. Saverina, V. Sivasankaran, R. R. Kapaev, A. S. Galushko, V. P. Ananikov, M. P. Egorov, V. V. Jouikov, P. A. Troshin and M. A. Syroeshkin, *Green Chem.*, 2020, **22**, 359–367.
9 Z. Yu, D. Wang, M. Lu, J. Li, X. Meng and H. Li, *Mater. Res. Bull.*, 2025, **182**, 113138.
10 C. K. Chan, X. F. Zhang and Y. Cui, *Nano Lett.*, 2008, **8**, 307–309.
11 L. Mei, M. Mao, S. Chou, H. Liu, S. Dou, D. H. L. Ng and J. Ma, *J. Mater. Chem. A*, 2015, **3**, 21699–21705.
12 J. H. Koo and S. M. Paek, *Nanomaterials*, 2021, **11**, 319.
13 H. Qiu, L. Zeng, T. Lan, X. Ding and M. Wei, *J. Mater. Chem. A*, 2015, **3**, 1619.
14 H. N. T. Nguyen, P. N. Ngoc, H. T. Huu, T. T. T. Phan, D. N. Nguyen, T. H. T. Nguyen, T. N. Van, L. N. Thi, M. K. Le, V. M. Tran, M. L. P. Le and V. Vo, *Chem. Phys. Lett.*, 2022, **801**, 139747.
15 T. Yoon, C. Chae, Y. K. Sun, X. Zhao, H. H. Kung and J. K. Lee, *J. Mater. Chem.*, 2011, **21**, 17325–17330.
16 J. R. Rodriguez, S. B. Aguirre, Z. Qi, H. Wang and V. G. Pol, *J. Colloid Interface Sci.*, 2024, **673**, 781–787.
17 X. Liu, T. Ji, T. Nie, T. Wang, Z. Liu, S. Liu, J. Zhao and Y. Li, *Mater. Lett.*, 2020, **261**, 127157.
18 C. Gao, N. D. Kim, R. V. Salvatierra, S. K. Lee, L. Li, Y. Li, J. Sha, G. A. L. Silva, H. Fei, E. Xie and J. M. Tour, *Carbon*, 2017, **123**, 433–439.
19 L. Qie, W. M. Chen, Z. H. Wang, Q. G. Shao, X. Li, L. X. Yuan, X. L. Hu, W. X. Zhang and Y. H. Hang, *Adv. Mater.*, 2012, **24**, 2047–2050.
20 D. H. Lee, D. H. Kim, H. C. Jung and C. M. Park, *Chem. Eng. J.*, 2023, **454**, 140329.
21 T. Kennedy, E. Mullane, H. Geaney, M. Osiak, C. O'Dwyer and K. M. Ryan, *Nano Lett.*, 2017, **14**(2), 716–723.
22 R. Ding, Y. Huang, G. Li, Q. Liao, T. Wei, Y. Liu, Y. Huang and H. He, *Front. Chem.*, 2020, **8**, 607504.
23 V. Nulu and W. S. Kim, *Korean J. Chem. Eng.*, 2015, **32**, 1918–1923.
24 A. Nulu, V. Nulu and K. Y. Sohn, *Korean J. Chem. Eng.*, 2020, **37**, 1795–1802.
25 W. Kaewraung and P. Hasin, *J. Energy Storage*, 2024, **82**, 110517.
26 Z. S. Wu, W. Ren, L. Xu, F. Li and H. M. Cheng, *ACS Nano*, 2011, **5**, 5463–5471.
27 L. G. Bulusheva, A. V. Okotrub, A. G. Kurenya, H. Zhang, H. Zhang, X. Chen and H. Song, *Carbon*, 2011, **49**, 4013–4023.
28 X. Ma, Y. Zhou, M. Chen and L. Wu, *Small*, 2017, **13**, 1700403.
29 C. R. Arro, A. T. I. Mohamed and N. Bensalah, *Mater. Today Commun.*, 2022, **30**, 103151.
30 A. Nulu, V. Nulu and K. Y. Sohn, *RSC Adv.*, 2024, **14**, 2564.
31 A. Nulu, V. Nulu, J. S. Moon and K. Y. Sohn, *Korean J. Chem. Eng.*, 2021, **38**, 1923–1933.
32 A. Verdianto, H. Jung and S. O. Kim, *Mater. Today Adv.*, 2024, **21**, 100472.
33 S. H. Choi, K. Y. Jung and Y. C. Kang, *ACS Appl. Mater. Interfaces*, 2015, **7**, 13952–13959.
34 L. Han, Q. Wei, H. Chen, J. Tang and M. Wei, *J. Alloys Compd.*, 2021, **881**, 160533.
35 F. Ma, S. Guan, D. Liu, Z. Liu, Y. Qiu, C. Sun and Y. J. Wang, *J. Alloys Compd.*, 2023, **940**, 168777.
36 B. Wang, J. Jin, X. Hong, S. Gu, J. Guo and Z. Wen, *J. Mater. Chem. A*, 2017, **5**, 13430–13438.
37 K. H. Seng, M. H. Park, Z. P. Guo, H. K. Liu and J. Cho, *Nano Lett.*, 2013, **13**, 1230–1236.
38 W. Lang, C. Yue, M. Dang, G. Wang, Y. Chen, F. Hu, Z. Liu and J. Shu, *J. Power Sources*, 2023, **560**, 232706.
39 S. Yan, H. Song, S. Lin, H. Wu, Y. Shi and J. Yao, *Adv. Funct. Mater.*, 2019, **29**, 1807946.
40 J. Y. Lee, D. T. Ngo and C. J. Park, *J. Korean Ceram. Soc.*, 2017, **54**, 249–256.

41 S. W. Kim, D. Ngo, J. Heo, C. Park and C. J. Park, *Electrochim. Acta*, 2017, **238**, 319–329.
42 E. Peled and S. Menkin, *J. Electrochem. Soc.*, 2017, **164**, A1703–A1719.
43 K. Xu, *Chem. Rev.*, 2004, **104**, 4303–4417.
44 M. N. Obrovac and V. L. Chevrier, *Chem. Rev.*, 2014, **114**, 11444–11502.
45 M. Nie, D. Chalasani, D. P. Abraham, Y. Chen, A. Bose and B. L. Lucht, *J. Phys. Chem. C*, 2013, **117**, 1257–1267.
46 V. Nulu, A. Nulu and K. Y. Sohn, *Nanoscale Adv.*, 2024, **6**, 3426.
47 K. D. Hyeon and P. C. Min, *Mater. Today Energy*, 2020, **18**, 100530.
48 T. Zeng, X. Liu, W. Kang, H. He, J. Zhang, X. Li and C. Zhang, *Angew. Chem., Int. Ed. Engl.*, 2021, **60**, 26218–26225.
49 D. J. Xue, S. Xin, Y. Yan, K. C. Jiang, Y. X. Yin, Y. G. Guo and L. J. Wan, *J. Am. Chem. Soc.*, 2012, **134**, 2512–2515.
50 F. F. Jia, L. X. Song, W. Wei, P. Qu and M. T. Xu, *New J. Chem.*, 2015, **39**, 689–695.